The 30° rotation domains in wurtzite ZnO films

Yu-Zi Liu[a], M.J. Ying[a], X.L. Du[a], J.F. Jia[a], Q.K. Xue[a],*, X.D. Han[b], Z. Zhang[b],*

[a]*Beijing National Laboratory for Condensed Matter Physics, Institute of Physics, Chinese Academy of Sciences, P.O. Box 603, Beijing 100080, China*
[b]*Beijing University of Technology, 100 Pingle Yuan, Chao Yang District, Beijing 100022, China*

Abstract

The 30° rotation domains in ZnO films were studied by transmission electron microscopy (TEM) and high-resolution electron microscopy (HREM). The cross-section and plane-view observations reveal that the 30° rotation domains have elliptical cylindrical shape, with the longitude axis along one of the $\langle 11\bar{2}0 \rangle$ directions and the short axis along one of the $\langle \bar{1}100 \rangle$ orientations, respectively. The volume fraction of the 30° rotation domains is about 1%. Due to the elliptical shape of the domain boundaries along the $[0001]_{ZnO}$ direction, partially disordered superlattice-like structures are formed. As shown by the HREM images and Zn elemental mapping, these super-lattices are most likely caused by periodical segregation and depletion of Zn along the domain boundary for compensating the mismatched lattice strain.

1. Introduction

Electrical and optical properties of GaN and ZnO films are largely affected by the defects such as threading dislocations, stacking faults, etc. [1]. *C*-plane ZnO and GaN films were usually prepared with mosaic-like structures on heterogeneous substrates [2,3]. When the ZnO and GaN thin films form on the surface of a substrate, the mosaic-like structures usually occur and the individual domain-island rotation around the [0001] would arise. The misorientation between the domain islands can lead to formation of tilt or rotation domains [3,4]. In these epitaxial films, rotation domains and/or inversion domains have been observed [5,6], which have great effects on the electronic structure of the films. Understanding and eliminating these detrimental effects by both experimental and theoretical efforts have attracted much attention in the past decade. Transmission electron microscopy (TEM) and

electron energy loss spectroscopy (EELS) have been used to study the microstructure and electronic structures with high spatial resolution [7]. Despite these efforts [4,8–14], a clear picture about the atomic structure of the large angle defect, for example the 30° rotation domain boundary, is still missing. In this paper we have particularly investigated the rotation domain and boundary structures in the ZnO epitaxial films grown on $(LaAlO_3)_{0.3}(Sr_{0.5}Ta_{0.5}O_3)_{0.7}$ (LSAT) (1 1 1) substrate, aiming to understand the atomic features of these domains and domain boundaries.

2. Experimental procedure

A radio frequency (RF) plasma assisted molecular beam epitaxy (MBE) system (OmniVac) was used to prepare the ZnO films on the LSAT (1 1 1) substrates. The Zn was supplied by evaporating elemental Zn (6N) from a commercial Knudsen cell, while a RF-plasma source (SVTA) was used to produce the active oxygen radicals. The gas flow rate was controlled by a mass flow controller (ROD-4, Aera).

---

*Corresponding authors. Tel.: +86 10 8264 8011.
  E-mail addresses: yzliu@blem.ac.cn (Y.-Z. Liu),
zhang@blem.ac.cn (Z. Zhang).

The substrates were degreased in trichloroethylene and acetone and rinsed with deionized water before introduced into the load-lock. After high temperature thermal cleaning and oxygen preconditioning of the substrate surface in UHV chamber, a conventional two-step growth method was used to prepare ZnO films, i.e., a low temperature buffer layer growth at $350\,^\circ$C and high temperature epilayer deposition at $650\,^\circ$C. The defects in the epitaxial films were studied by TEM (Philips CM200 FEG and TECNAI F20 operating at 200KV). The cross-section specimen was prepared by standard procedures including cutting, mechanically polishing, dimple grinding, and low angle ion milling. For preparation of the plan-view specimens, only mechanical polishing to a thickness of $50\,\mu$m was performed on the substrate side, followed by dimple grinding to a thickness of about $15\,\mu$m. The final foil was prepared by further back thinning at 3° from the substrate side until hole appeared. In order to avoid the contamination, thin mica sheet was used to protect the ZnO film.

3. Results and discussion

3.1. General view of the domain structure from the cross-section view of the specimen

(La,Sr)(Al,Ta)O$_3$ (LSAT) with a mixed perovskite structure was developed mainly as a substrate for high Tc superconductivity film growth at the beginning [15]. The atomic structure has been investigated [16]. Recently, LSAT(1 1 1) was also used as a promising substrate for III-nitride films, because the lattice mismatch between GaN and LSAT(1 1 1) is theoretically less than 1% with the epitaxial relationship of $[0\,0\,0\,1]_{GaN}||[1\,1\,1]_{LSAT}$ and $[1\,1\,\bar{2}\,0]_{GaN}||[1\,1\,\bar{2}]_{LSAT}$ [17,18] and the C6 symmetry in the $(1\,1\,1)_{LAST}$ plane. The perovskite structure has C3 symmetry, but C6 here only indicates the symmetrical features of (1 1 1) plane of the material. The epitaxy ZnO film has C6 symmetry on the (0 0 0 1) plane to accommodate the C6 symmetry features of (1 1 1) plane of LAST. In our growth experiments, LSAT(1 1 1) was also used as the substrate for ZnO expitxy. But the complex atomic configuration of the $(1\,1\,1)_{LAST}$ plane makes the preparation of a perfect epitaxial film difficult. The epitaxial orientation relationship between the ZnO film and LSAT substrate was investigated in our previous study [6]. The main epitaxial relationship is $(0\,0\,0\,1)_{ZnO}||(1\,1\,1)_{LSAT}$ and $[1\,1\,\bar{2}\,0]_{ZnO}||[\bar{1}\,1\,0]_{LSAT}$ [6]. There are two kinds of epitaxial orientation relationships between ZnO and LSAT substrate with different lattice mismatches (18.9% and 2.9%). Normally, both two kinds of domains can form in ZnO films with different interfacial configurations. There is a 30° in-plane rotation between these two domains. The rotation domain boundaries formed in the ZnO films can be clearly observed in the cross-sectional TEM dark field images as shown in Fig. 1. Figs. 1(a) and (b) are the two-beam dark field images of a cross-section specimen with the operation
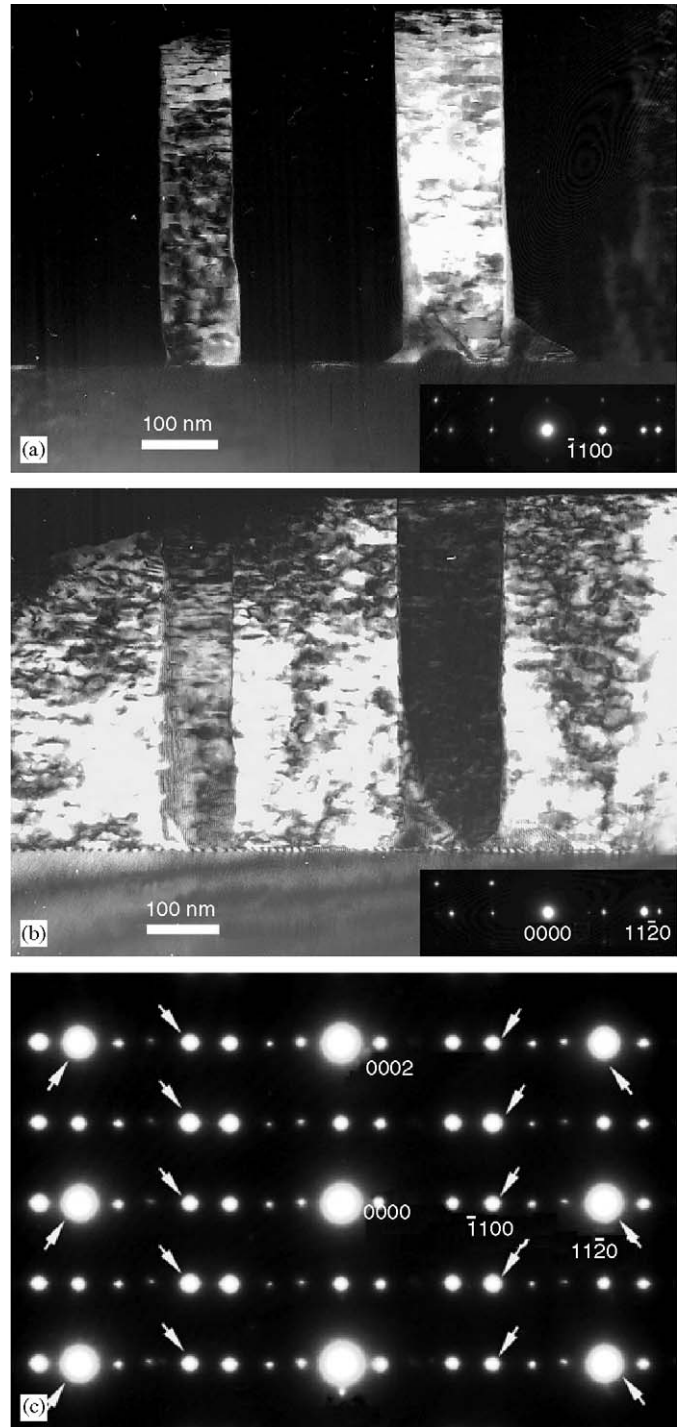

Fig. 1. Dark field images with reflections of (a) $g = (\bar{1}\,1\,0\,0)$ and (b) $g = (1\,1\,\bar{2}\,0)$, respectively. The bottom-inserted images indicate the two beam conditions; (c) is the selected area electron diffraction pattern covering the two domain regions.

reflectors $\mathbf{g} = (\bar{1}\,1\,0\,0)$ and $(1\,1\,\bar{2}\,0)$, respectively. The two beam situations are shown in the inserted images. From Figs. 1(a) and (b) we can find that the contrast is inverted under the two reflector's operations. As more clearly shown by the plane-view observation in the following section, these two domains have a 30° $(0\,0\,0\,1)_{ZnO}$ in-plane
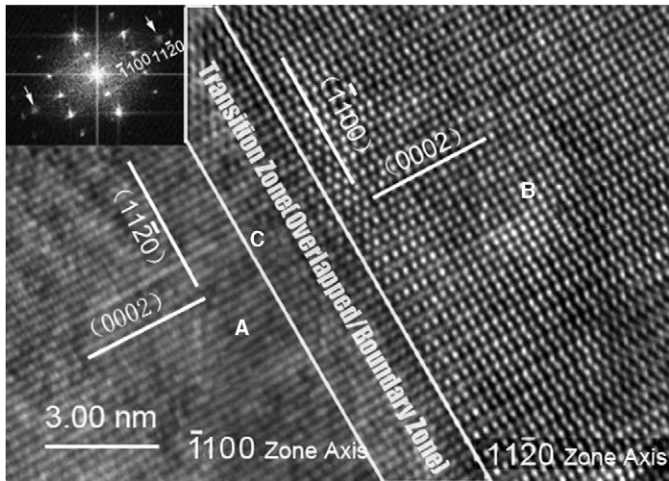
Fig. 2. The HREM image of the cross-section view specimen near the rotation domain boundary. There is a transition zone C between the two domains A and B. The insert is the FFT pattern of the HREM image.
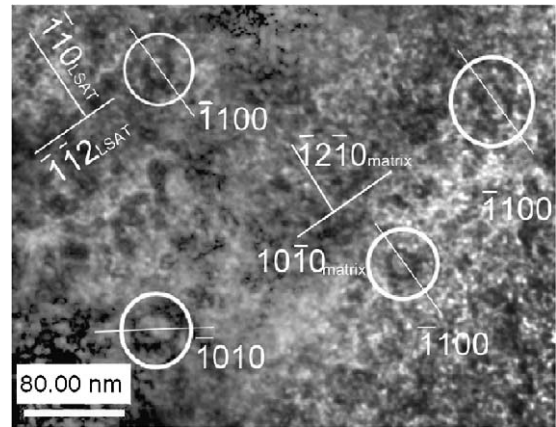

Fig. 3. The low magnification bright filed image of the plane-view specimen. The open white circles indicate the elliptical rotation domains which randomly distribute in the matrix. The longitude axis of the ellipse is along the $(\bar{1}100)$ plane.

rotation. The two $30°$ (0001) in-plane rotation domains co-exist and have a planar crystallographic relationship of: $(0001)_{\text{Rotation domain}}\|(0001)_{\text{Main domain}}\|(111)_{\text{LSAT}}$. Fig. 1(c) shows the diffraction pattern taken from the area covering the two domain regions. There are not only two sets of main diffraction spots from the two domains but also additional weak points distributed around the main diffraction pattern. Such diffraction pattern is explained in terms of the ordered structures near the domains' boundary of the observed area. The up-pointing and down-pointing arrows indicate the diffractions from the bright strips in Fig. 1(a) and (b), respectively. The extra weak spots are due to multiple diffractions [19].

Fig. 2 shows the cross-section HREM image of the rotation domain. The electron beam was along the $[11\bar{2}0]$ azimuth of domain B on the right. The lattices can be resolved clearly with the 0.2 nm resolution limit of the electron microscope. The electron beam direction is parallel to the $[\bar{1}100]$ azimuth of domain A on the left side. The top insert shown in Fig. 2 is the fast Fourier transform (FFT) pattern of this HREM image. The scattering spots indicated by the two arrows are from the $(11\bar{2}0)$ planes of the left domains. The area C in Fig. 2 is a transition zone. The blurred contrast of area C derives from the overlapped lattices of the two domains around the boundary. The transition from the right lattice to the left striation is not so sharp. In fact, the domain A possesses an elliptical shape along the $[0001]$ observing direction, and this transition zone is caused by the curved boundary of the rotation domain, which can be clearly revealed in the plane-view images discussed below.

3.2. The domain boundary structure along the [0001] observing direction

To further understand the details of the domain boundary structure, the plane-view observation was carried out, which enables the domain boundary to be studied by an edge on state, i.e. the observation can be carried out along the $[0001]_{\text{ZnO}}$ azimuth. Fig. 3 shows a bright field image at low magnification, from which the distribution of the rotation domains can be seen. Some of the lattice plane indices are indicated in the figure. The small areas marked by the white open circles in Fig. 3 are the rotation domains. Here we use R to denote the minority rotation domains, i.e. the small white-circled areas, and M for the majority domains. Because of the continuity of the single-crystal-like domain M, domain R can be simply regarded as defects in the domain M matrix. They are randomly distributed in domain M. Obviously the probability of forming these two domains is not equal. The area fraction of domain R over matrix M can be simply calculated to be $r = S_R/S_M = S_A/(S-S_R) = 0.01$. S_R is the area of the four R domains, S_M is the area of domain M, and S is the total observed area. The volume fraction of the rotation domain R is very small. The rotation domain R has an elliptical shape approximately. The longitude axis of the $30°$ rotation domain R is along the $[11\bar{2}0]$, and the short axis is along $[\bar{1}100]$ as shown in Fig. 4. The elliptical shape of the R domain may derive from the energy anisotropy along $[\bar{1}100]$ and $[11\bar{2}0]$ directions of ZnO. The binding energy between ZnO and LSAT is different between the $[\bar{1}100]$ and $[11\bar{2}0]$ directions on the $(0001)_{\text{ZnO}}/(111)_{\text{LAST}}$ planes.

There are three equivalent long axis directions of domain R because both the $(0001)_{\text{ZnO}}$ and $(111)_{\text{LSAT}}$ have the same C6 symmetry. Two variants can be revealed in the plane-view image in Fig. 3. The $(\bar{1}100)$ plane of one variant of R domains is parallel to the $(\bar{1}10)$ plane of the LSAT substrate and the $(\bar{1}2\bar{1}0)$ matrix-domain. One of the R domains shown in Fig. 3 was magnified until the lattice structure can be clearly revealed. The top right inset is the FFT pattern of the HREM image. There are two sets of diffraction spots from the two domains with a $30°$ $(0001)_{\text{ZnO}}$ in-plane rotation. The clear in-plane boundary
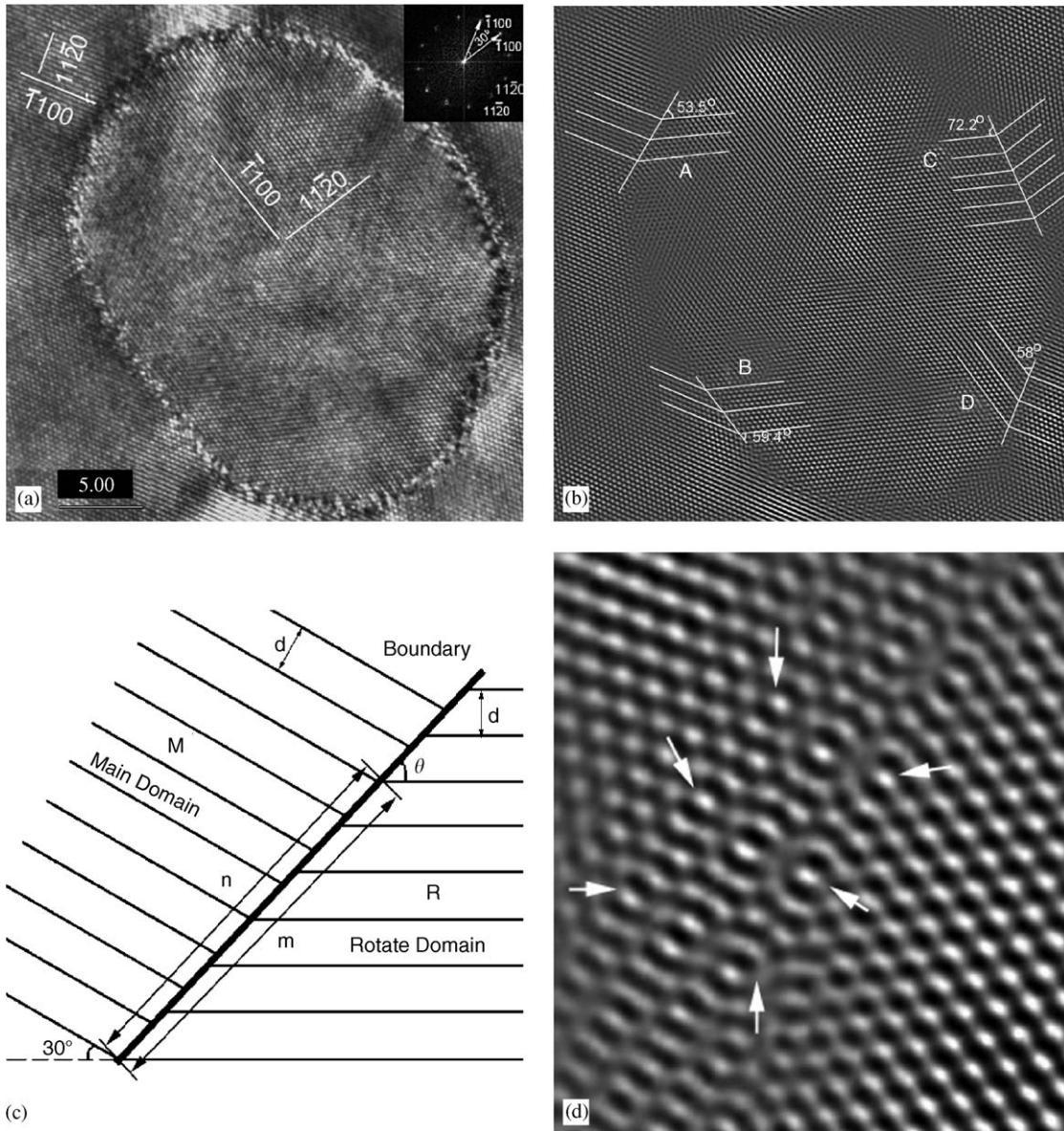
Fig. 4. (a) The in-plane HREM image of a rotation domain in the specimen. The top-right insert is the FFT pattern of this image; (b) is the Fourier filtered image of (a), the angles describe the localized geometrical features of the domain boundary with the $(1\bar{1}00)$ planes of the R domain; (c) is the model to explain the lattice mismatch variation with changing the angle θ, see text for details; (d) is the enlarged image of area A of (b), the arrows indicate the super lattice spots.

between the two domains is revealed. We note that the structure of the domain boundary is non-uniform. There are different lattice configurations between these two domains at different situations. In order to understand the lattice match configurations, Fig. 4(a) was filtered through the reverse Fourier transformation by only selecting the main diffraction spots from the two domains. The filtered Fourier image is shown in Fig. 4(b). Four areas marked by A, B, C and D along the domain boundary were analyzed. The mismatched lattice features are different in the four regions when the localized geometrical configuration varies. The domain boundary structure is closely related to the relative orientation of the two lattice planes of the two domains with the localized features of the

domain boundary. Here, we use θ to define the angle between the tangential direction of the curved boundary and the $(\bar{1}100)$ lattice plane of domain R and use it to describe the localized domain boundary feature. The corresponding localized lattice plane of domain R has a $30°$ rotation about $[0\,0\,0\,1]$ axis relative to domain M. Considering the inter-penetrated lattices of domain R and M in the two dimensional case, such as the two sets of $(\bar{1}100)$ planes of domain R and M, with varies angle θ, the localized match and mismatch features will be different. The geometrical configurations of the domain boundary are shown in Fig. 4(c). m and n are the corresponding matched lattice numbers of domain R and M, i.e., m lattice planes of domain R travel the same distance with n lattice

Table 1
The geometrical configurations of lattice mismatch at *A*, *B*, *C* and *D* regions

Locations	m	n	$\theta_{exp}(°)$	$\theta_{cal}(°)$
A	4	5	53.5	52.4
B	5	3	59.4	62.0
C	5	6	58.0	56.3
D	3	3	72.2	75.0

See text for detail descriptions of *m, n* and *θ*.

planes of domain *M* along domain boundary. They have the following relationship:

$$\operatorname{ctg} \theta = \frac{2n}{m} - \sqrt{3}. \tag{1}$$

Table 1 shows the calculated and observed experimental angle *θ* as well as the lattice match number *m* and *n* between domains *R* and *M*. The *A*, *B*, *C* and *D* show the equivalent $(\bar{1}100)$ plane lattice configurations between domains *R* and *M*. The experimental observed angles *θ* agree well with the calculated ones. There are various super-lattice-like features along the domain boundary in regions *A*, *B*, *C* and *D*. An example for area *A* was magnified, as shown in Fig. 4(d). A typical super-lattice structure is revealed. The arrows in Fig. 4(d) highlight some of the lattice points located at the super-lattice. One of the periods of the constructed super-lattice is 1.1 nm which is four times of the *d*-space of $(\bar{1}100)$ plane. We speculate that the super-lattice structure along the domain boundary comes from the re-ordering of the Zn element along the domain boundary, which is driven by the strain-field of the mismatched lattices. The HREM simulation was conducted on a basis ZnO structure. Fig. 5(b) shows the simulated ZnO HREM along the (0001) zone axis with depleting two Zn atomic columns based on the model in Fig. 5(a). According to this pair of simulations, the bright spots in the HREM image in Fig. 4(a) can be interpreted to be the depleted Zn atoms along those atomic columns.

3.3. Re-ordering of Zn element on the domain boundary

To confirm the re-ordering of Zn element along the domain boundary, elemental mapping for Zn was done on one of the domain areas by applying the energy filtered TEM. In this experiment the three window method [20] was applied to obtain the Zn elemental mapping (see Fig. 6). The black and white contrast measures the quantity of the Zn element. *Brighter* regions correspond to the Zn *enriched* regions while the *dark* ones the *poor* Zn regions. A periodic Zn distribution is observed along the domain boundary, as indicated by the white arrows in Fig. 6. The Zn re-ordering period is about 1 nm which is consistent with the 1.1 nm super-lattice period observed in the HREM image. The super-lattices along the domain boundary are most likely
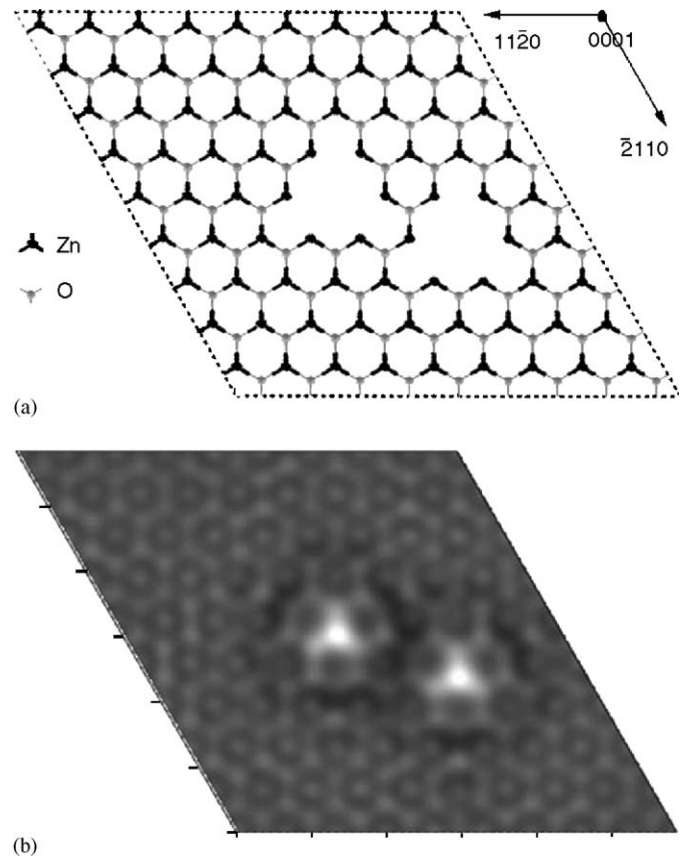

(a)

(b)

Fig. 5. The simulated HREM image of the Zn depleted structure: (a) is the atomic structural model and (b) is the simulation HREM image based on the model shown in (a).
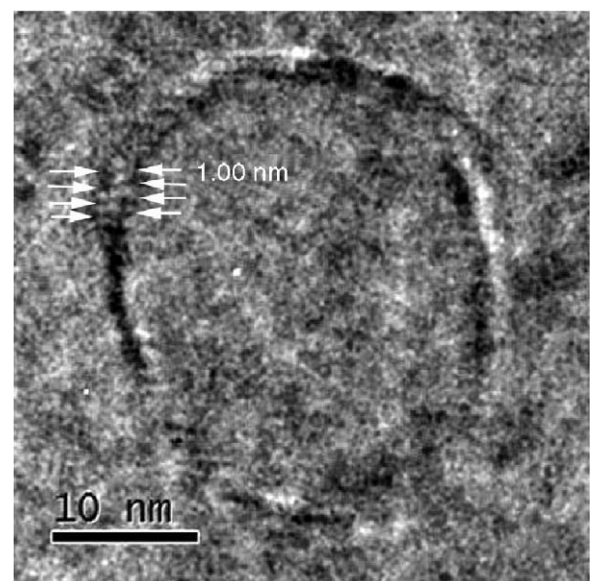

Fig. 6. Energy filtered Zn element mapping including both of *R* and *M* domains.

due to the periodical segregation and depletion of Zn element along the domain boundary to compensate the mismatched lattice strain.

4. Summaries

On the basis of the cross-section and plan-view observations by TEM and HREM, we have shown that the 30° rotation domains (defined to be R domain in this study) possess elliptical cylindrical shape. The longitude axis of the R domain is along one of the $\langle 11\bar{2}0 \rangle$ directions of ZnO. There should be three equivalent R domain variants. One of the domain variants has its longitude axis roughly parallel to the $[\bar{1}10]$ direction of the LSAT substrate. The volume fraction of the R domain is very small (about 1%). Crystallographically non-uniform domain boundary structure is observed. The lattice configuration of the domain boundary is related to the relative angle between the lattice planes and domain boundary. The strain from the lattice mismatch contributes to the super-lattice like features and the semi-periodical re-ordering of Zn element around the domain boundary.

References

[1] V. Srikant, D.R. Clarke, J. Appl. Phys. 81 (1997) 6357.
[2] V. Srikant, J.S. Speck, D.R. Clarke, J. Appl. Phys. 82 (1997) 4286.
[3] F. Vigué, P. Vennéguès, C. Deparis, S. Vézian, M. Laügt, J.-P. Faurie, J. Appl. Phys. 90 (2001) 5115.
[4] V. Potin, P. Ruterana, G. Nouet, R.C. Pond, H. Morkoc, Phys. Rev. B 61 (2000) 5587.
[5] A.M. Sánchez, P. Ruterana, M. Benamara, H.P. Strunk, Appl. Phys. Lett. 82 (2003) 4471.
[6] Yu-Zi Liu, M.J. Ying, X.L. Du, Z.Q. Zeng, Z.X. Mei, J.F. Jia, Q.K. Xue, Z. Zhang, Phys. Lett. A 339 (2005) 497.
[7] D.A. Muller, T. Sorsch, S. Moccio, F.H. Baumann, K. Evans-Lutterodt, G. Timp, Nature (London) 399 (1999) 758.
[8] X.J. Ning, F.R. Chien, P. Pirouz, J.W. Yang, M. Asif Khan, J. Mater. Res. 11 (1996) 580.
[9] L.T. Romano, J.E. Northrup, M.A. O'Keefe, Appl. Phys. Lett. 69 (1996) 2394.
[10] V. Potin, P. Ruterana, G. Nouet, J. Appl. Phys. 82 (1997) 2176.
[11] J.E. Northrup, J. Neugebauer, L.T. Romano, Phys. Rev. Lett. 77 (1996) 103.
[12] Y. Yan, M.M. Al-Jassim, Phys. Rev. B 69 (2004) 0085204.
[13] A. Béré, A. Serra, Phys. Rev. B 66 (2002) 085330.
[14] F. Oba, H. Ohta, Y. Sato, H. Hosono, T. Yamamoto, Y. Ikuhara, Phys. Rev. B 70 (2004) 125415.
[15] B.C. Chakoumakos, D.G. Schlom, M. Urbanik, J. Luine, J. Appl. Phys. 83 (1998) 1979.
[16] H. Li, L. Salamanca-Riba, R. Ramesh, J.H. Scott, J. Mater. Res. 18 (2003) 1698.
[17] A. Atshagiri, C. Niederberger, A.J. Francis, L.M. Porter, P.A. Salvador, D.S. Sholl, Surf. Sci. 537 (2003) 134.
[18] M. Sumiya, T. Chikyow, T. Sasahara, K. Yoshimura, J. Ohta, H. Fujioka, S. Tagaya, H. Ikeya, H. Koinuma, S. Fuke, Jpn J. Appl. Phys. 41 (2002) 5038.
[19] P.B. Hirsch, A. Howie, R.B. Nicholson, D.W. Pashley, M.J. Whelan, Electron Microscopy of Thin Crystals, Robert E. Krieger Publishing Co, Malabar, FL, 1977, p. 358, 361.
[20] F. Hofer, P. Warbichler, W. Grogger, Ultramicroscopy 59 (1995) 15.